


Phase-Incoherent Photonic Molecules in V-Shaped Mode-Locked Vertical-External-Cavity Surface-Emitting Semiconductor Lasers

Jan Hausen^{1,*}, Stefan Meinecke¹, Julien Javaloyes², Svetlana V. Gurevich^{2,3} and Kathy Lüdge¹

¹*Institute for Theoretical Physics, Technische Universität Berlin, Hardenbergstraße 36, 10623 Berlin, Germany*

²*Departament de Física, Universitat de les Illes Balears & Institute of Applied Computing and Community Code (IAC-3), Cra. de Valldemossa, km 7.5, E-07122 Palma de Mallorca, Spain*

³*Institute for Theoretical Physics, University of Münster, Wilhelm-Klemm-Str. 9, 48149 Münster, Germany*

 (Received 26 May 2020; revised 1 September 2020; accepted 25 September 2020; published 30 October 2020)

Passively mode-locked vertical external-cavity surface-emitting semiconductor lasers (VECSELs) composed of a gain chip and a semiconductor saturable absorber have been drawing much attention due to their excellent performance figures. In this work we investigate how localized structures and incoherent, non-locally bound, pulse molecules emerge in a long cavity VECSEL using a V-shaped cavity geometry. We show that these states are bistable with the laser off state and that they are individually addressable. Using a model based upon delay differential equations, we demonstrate that pulse clusters result from the cavity geometry and from the nonlocal coupling with the gain medium; in the long cavity regime this leads to locally independent, yet globally bound, phase incoherent photonic molecules. Using a multiple timescale analysis, we derive an amplitude equation for the field that allows us to predict analytically the distance between the elements of a cluster.

DOI: [10.1103/PhysRevApplied.14.044059](https://doi.org/10.1103/PhysRevApplied.14.044059)

I. INTRODUCTION

Vertical external-cavity surface-emitting semiconductor lasers (VECSELs) composed of a gain chip and a semiconductor saturable absorber mirror are an important class of passively mode-locked (PML) lasers [1]. These devices are able to generate transform-limited pulses in the 100 fs range with peak powers of 500 W [2] at GHz repetition rates. In the limit of cavity round trips much longer than the gain recovery time, typically a nanosecond in semiconductor materials, the mode-locked pulses found in VECSELs may coexist with the off solution. In these conditions, they can be interpreted as *temporal localized structures* (LSs) [3]. This regime can be leveraged to generate PML states composed of individually addressable pulses at arbitrary low repetition rates, using, e.g., current or optical modulation [4–7].

Localized structures are ubiquitous in dissipative systems and they have been widely observed in nature [8–16], as well as in a variety of driven photonic nonlinear systems such as ring resonators [5,17], microcavities [18], and external cavities fed by a vertical cavity surface emitting lasers [19,20]. Because of the extension of the original concept of conservative solitons, LSs are also sometimes referred to as dissipative solitons [21,22]. In photonic systems LSs occur either transversely to the propagation

direction [23,24] or in the longitudinal (temporal) direction [3,6,25–27]. Localization in both directions would potentially lead to light bullets [28–31].

In this paper we focus on the dynamics of temporal LSs found in VECSELs arranged in a V-shaped cavity configuration [2,32–34]. At variance with previous works that employed linear cavities, the gain chip in the case of the V-shaped configuration is positioned between the absorber and the output mirror. In addition to the LSs that also exist in linear cavities, the V-shaped geometry induces phase-incoherent photonic molecules, i.e., pulses that are globally bound but locally independent. Their temporal separation can be controlled by tuning the difference in the optical path between the two arms of the “V” as pulses pass through the gain section twice per round trip inducing the necessary nonlocal influence. In the long cavity regime, these can be referred to as weakly bound “catenane molecules” like those found recently in Refs. [35,36]. Similar molecular soliton structures have also been examined using Kerr cavities [37], mode-locked fibre lasers [38–40], or optical fibres pumped by solid-state lasers [7,41–44].

Temporal localization in photonic systems can be taken advantage of to realize a variety of applications [22]. In particular, LSs can be used as elementary bits of information while the cavity acts as an all-optical buffer [3,45–48]. With regard to optical communications, soliton molecules have been suggested to extend the binary alphabet to enhance optical data transfer by transferring

*hausen@campus.tu-berlin.de

several bits simultaneously to circumvent the Shannon limit [49–51]. Individual addressing opens further interesting possibilities for the optical generation of arbitrary trains of spikes, which has potential applications in different domains. Because of the observed incoherence between pulses inside a single molecule, they could be applied in future spectroscopy applications demanding dense frequency combs but a variable distribution of the comb power [52–55]. Here, since the various pulses do not generate a coherent beating, the comb would not be spectrally modulated. The intensity of the teeth in the comb would scale with the number of pulses, while avoiding the resolution decreases incurred by having N pulses in the cavity which usually leads to an N -fold increase of the comb spacing. This might also find applications in pump-probe sensing of material properties [56]. Furthermore, the possibility to create specific, stable pulse patterns from a single device can also be of use for material processing [57].

As mode-locked VECSEL optical systems have a wide array of applications, further understanding their dynamics as a function of the cavity parameters to improve the performance or prevent certain dynamical regimes is essentially a topic relevant to applied physics. As such, the possibility to generate controllable clusters of LSs using nonlocal effects has both fundamental and practical interests.

II. EMERGENCE OF LSs

The setup of a V-shaped passively mode-locked VECSEL is sketched in Fig. 1. There, the gain chip is placed in a central position while the semiconductor saturable absorber and the output coupler are located on each side of the cavity. A single pulse depletes the gain twice during one round trip as it propagates forward and then backward through the cavity [black arrows in Fig. 1(a)]. The cavity configuration can be described by the length of the two cavity arms $\tau_1 = L_1/c$ and $\tau_2 = L_2/c$.

As in the experimental realization in Refs. [2,32], we model our system with the delay differential equations (DDEs) derived in Appendix A of Ref. [33] and based upon Ref. [58]. The theoretical model yields the dynamics of the electric field E and the integrated carrier densities of the saturable absorber Q and of the gain G as

$$\dot{E} = -\gamma E + \gamma E(t-T)R(t-T), \quad (1)$$

$$\begin{aligned} \dot{G} = & \gamma_g(G_0 - G) - (e^G - 1) \\ & \times \{|E|^2 + |E(t-2\tau_2)|^2 e^{G(t-2\tau_2)-2Q(t-2\tau_2)}\}, \end{aligned} \quad (2)$$

$$\dot{Q} = \gamma_q(Q_0 - Q) + s(e^{-2Q} - 1)e^G |E|^2, \quad (3)$$

$$R(t) = \sqrt{\kappa} e^{(1-i\alpha_g)[G(t+2\tau_2)+G(t)]/2 - (1-i\alpha_q)Q(t)}, \quad (4)$$

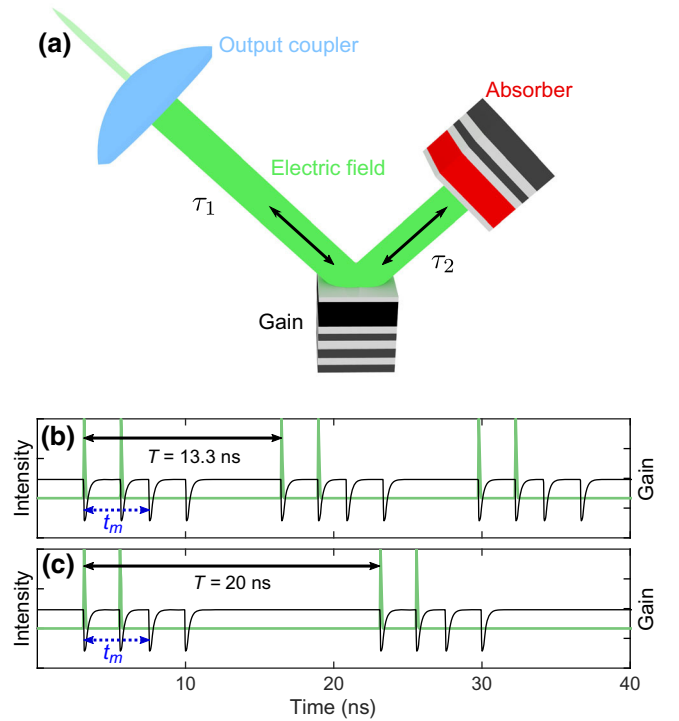


FIG. 1. Setup of a passively mode-locked VECSEL with V-shaped cavity geometry. The main constituents are a semiconductor saturable absorber mirror, an out-coupling facet with high reflectivity ($\kappa \approx 0.99$), and a semiconductor gain chip that can be optically or electrically pumped. The time of flights in the two cavity arms are τ_1 and τ_2 . (b),(c) Photonic molecules in the long cavity limit for fixed $\tau_2 = 2.2$ ns but at varied cavity length T , with t_m referring to the size of the molecule.

where γ describes the resonance width of the gain chip, $\gamma_{g,q}^{-1}$ are the carrier lifetimes in the gain and the absorber section, G_0 is the unsaturated gain driven by the pump power, Q_0 is the unsaturated absorption in the absorber chip, κ models the nonresonant losses per round trip, the factor r_s is proportional to the ratio of the differential gain coefficients and confinement factors in the two active sections, and $\alpha_{g,q}$ are the linewidth enhancement factors in the gain and absorber section, respectively. The algebraic equation (4) describes the total amplification and losses of the electric field during one round trip in the laser cavity. We note that the cold cavity round-trip time is $T = 2(\tau_1 + \tau_2)$ (see Fig. 1), such that $\tau_1 = \tau_2 = 0.25T$ describes the symmetric V-shaped cavity. We note that we have applied a coordinate transformation of the time t , to reduce the number of delayed terms (see the detailed explanation in Appendix A).

We use a set of standard parameters depicted in the caption of Fig. 2 to analyze the system in the long cavity regime below the lasing threshold, i.e., we set G_0 such that $G_0 < G_{th}$, where $G_{th} = Q_0 - \frac{1}{2} \log \kappa$ is the continuous-wave lasing threshold. This means that single pulses can

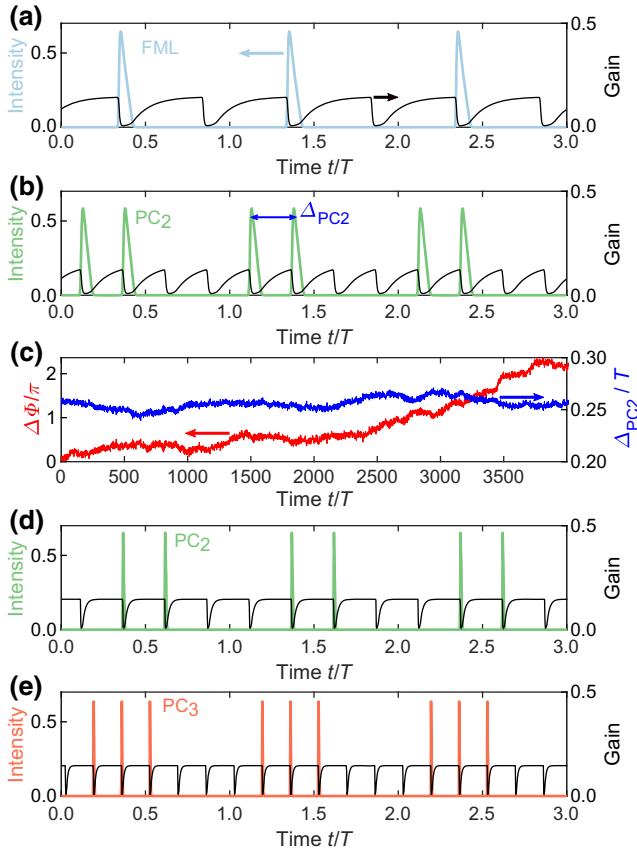


FIG. 2. Localized structures (colored pulses) and the corresponding evolution of the gain G (black lines) in the intermediate and long symmetric cavity regime found by direct numerical integration of Eqs. (1)–(4). (a) Single pulse regime; a secondary ghost gain depletion corresponding to the second gain pass is clearly visible. (b) Pulse cluster with two elements (PC_2). (c) Phase difference between the two elements of the PC_2 bound state $\Delta\phi$ (in red). It is freely drifting while the relative distance (Δ_{PC_2} in blue) between the two bits remains constant, up to the influence of noise. In all cases presented in (a)–(c) $T = 1.875$ ns. (d) Evolution of the PC_2 state in the long cavity regime $T = 12.5$ ns and (e) PC_3 dynamics with $T = 25$ ns. Other parameters are $\gamma_g = 5$ ns $^{-1}$, $\gamma_q = 180$ ns $^{-1}$, $Q_0 = 0.177$, $\gamma = 240$ ns $^{-1}$, $G_0/G_{th} = 0.8$, $\kappa = 0.99$, $s = 20$, and $\alpha_{g,q} = 0$. For (c), $\alpha_g = 1.5$, $\alpha_q = 0.5$, and the noise is added as $\sqrt{(\eta/dt)}D$ in each integration step for Eq. (1), with Gaussian white noise term D and noise strength $\eta = 25$ (normalized to T).

be individually excited while being multistable with the homogeneous “off” solution [3,6,26,27]. At this point we emphasize that the general appearance of a localized structure is not affected by the amplitude phase coupling and, therefore, we set $\alpha_{g,q} = 0$ in the first steps of our study [3].

In general, pulses interact with each other via the overlap of their tails and, at long range, the slowest variable to relax is the gain material one, i.e., $G(t)$ relaxes on the timescale of γ_g^{-1} . Repulsive interactions between

pulses stem from the gain exponential tails [4,59], thereby favoring an equidistant pulse spacing, which leads to harmonic mode locking (HML). The relaxation towards equidistant pulses in the HML solutions can be arrested by using a sufficiently long cavity. More precisely, the transitory time can be made exponentially large. Therefore, we set $\gamma_g T \gg 1$. Because of the double gain pass of a single pulse during each round trip in the V-shaped cavity [Fig. 1(a)], additional pulse depletions appear. In the long cavity limit a second pulse can be trapped in between the two gain depletions of the preceding pulse, as indicated by the blue dashed arrows in Figs. 1(b) and 1(c). In this molecule structure (photonic molecule), the second pulse is locally independent as the gain completely relaxes between the passes of the two pulses, but globally bound by the second gain depletion of the preceding pulse. In this situation the size of the molecule t_m is only dependent on the smaller delay $\min(\tau_2, \tau_1)$ and not on the size of the complete resonator T , as indicated in Figs. 1(b) and 1(c); it is because $\min(\tau_2, \tau_1)$ governs the timing of the second gain depletion.

Similarly to the LSs investigated in face-to-face coupled cavities [3,4,6], we find that LSs can be triggered in subthreshold V-shaped cavities, and that the latter are multistable to the “off” solution; see Fig. 2(a) and Appendix B. However, a unique characteristic of the V-shaped cavity, i.e., a second gain pass per round trip, leads to a secondary gain depletion as observed in Fig. 2(a) that seems to be triggered by a “ghost” pulse (see Appendix A). The gain temporal profile in Fig. 2(a) highlights how a single pulse can induce (apparent) nonlocal effects in the active material as pointed out in Refs. [32,33]. In addition, the nonlocal gain dynamics allows the creation of a pulse cluster of n pulses (denoted PC_n). An example of such a regime is depicted in Fig. 2(b) in the intermediate cavity regime ($T = 1.875$ ns); as each pulse creates two depletions of the gain (shown in black), the latter is not able to fully recover to the equilibrium; therefore, the pulses within a cluster are strongly bound in this case. This can be asserted by representing the behavior of their relative distance Δ_{PC_2} [see the blue line in Fig. 2(c)]; while it fluctuates around an equilibrium value of $\Delta_{PC_2} \simeq 0.25T$, it does not converge to that of an harmonic mode-locking solution $\Delta_{HML_n} \simeq T/n$ [59]. However, the relative phase between the elements of a cluster is free to drift; see the red line in Fig. 2(c). Averaging over different noise realizations, we find that the ensemble variance of the phase grows linearly with time, revealing a diffusive behavior. These results convincingly prove that the LSs forming clusters are not phase coherent one with each other and therefore can be identified as phase incoherent photonic molecules.

The PC solutions persist in a long cavity regime, as shown in Figs. 2(d) and 2(e). Here the gain relaxes to its equilibrium in-between pulses. This leads to a scenario in which the second pulse is locally independent from

the first pulse due to the flat gain landscape between the first pulse and its ghost image (second gain pass) in the middle of the round trip. Yet, the second pulse cannot approach the ghost replica as it would encounter a depleted gain, which generates repulsive forces. As such, the second pulse is globally bound due to the nonlocal dynamics of the gain; such a mechanism is similar to that of the nested molecules found in Refs. [25,35,40]. In this case the size of the molecule is only dependent on the distance between the two gain passes of one pulse. At even higher round-trip times ($T = 25$ ns), similar higher-order locally independent yet globally bound PCs can be observed; the PC₃ solution is shown in Fig. 2(e). Here also, although the pulses are bound within a cluster, they are mutually incoherent. Note that multipeak bound structures also exist in ring mode-locked cavities, but only as unstable solutions and with varying pulse amplitudes among the structures [60] or induced by a periodic excitation scheme [6].

Utilizing the path continuation software DDE-Biftool [61], we can gain a deeper insight into the behavior and dynamics of the harmonic mode-locking solutions and pulse clusters in or near the localized regime. The maximum intensity for the different branches of harmonic solutions as a function of the pump power G_0 are represented in Fig. 3(a), while the corresponding temporal outputs are depicted in Figs. 3(b₁₋₄) in matching color. Similar to the results obtained for face-to-face coupled cavities [3,6,60], equally spaced temporal LSs are generated via Andronov-Hopf bifurcations along the continuous-wave (cw) branch continued in pump power G_0 . The fundamental mode-locking (FML) and harmonic mode-locking (HML_{*n*}) solution branches, distinguished by the number n of pulses in the cavity, emerge subcritically; this means that they appear as unstable solution branches—see the thin lines in Fig. 3(a). The branches then fold at a saddle node (SN) bifurcation point [labeled with squares in Fig. 3(a)]. Furthermore, they may give rise to a stable solution; see the thick lines in Fig. 3(a). It is by this mechanism that the various regimes exist below the cw threshold, i.e., $G_0 < G_{th}$. All these solution branches are therefore multistable with the off solution, which is an essential criterion for the pulses to become localized [3,22].

The FML solution stabilizes at the SN point. However, the HML solutions become stable in torus (tr) bifurcations (labeled with circles) occurring at pump currents slightly above the respective SN points [see Fig. 3(a)]. This stabilization mechanism is different from the case of a face-to-face coupled cavity, where all solutions would stabilize at their respective SN points [3,60]. In the symmetric cavity configuration chosen in Fig. 3, the regular temporal separation between pulses in the harmonic solutions HML₂ and HML₄ make it so that one can find only as many gain depletions as there are pulses, and not twice as much as for the HML₃ branch. In the former case each gain depletion results from the combined effect of the influence of a pulse

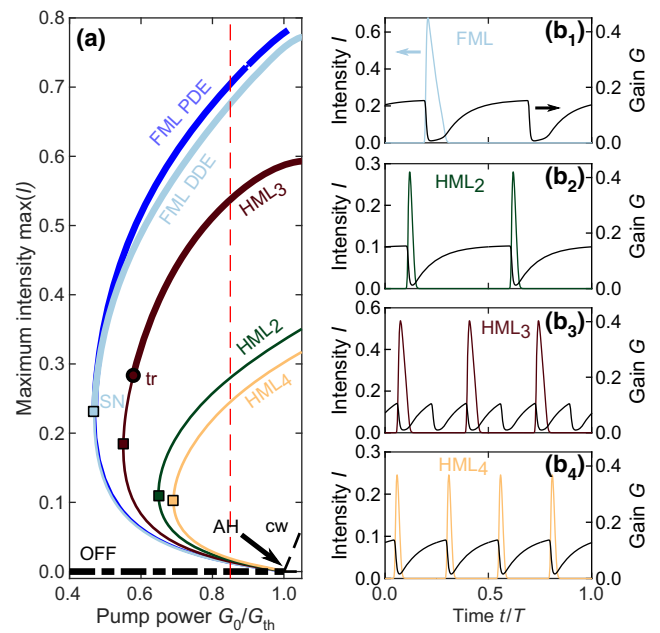


FIG. 3. (a) Evolution of the maximum pulse intensity with respect to the normalized pump power G_0/G_{th} of the fundamental mode-locking (FML) and harmonic mode-locking (HML_{*n*}) solutions, where subscript n denotes the number of equally spaced pulses. Thick and thin lines indicate stable and unstable dynamics, respectively. The solutions are born in subcritical Andronov-Hopf bifurcations along the steady-state cw branch (intensity stretched by a factor of 40). The FML branch is found utilizing the path continuation of the DDE model (1)–(3) (light blue) and the Haus master equation (4) (dark blue). The branches all fold back in saddle-node bifurcations (squares) and become multistable to the off solution depending on the cavity geometry. The HML₃ solution stabilizes in a torus (tr) bifurcations (circle). (b₁₋₄) Gain and field intensity profiles at $G_0/G_{th} = 0.85$ [marked by a dashed line in (a)] and symmetric cavity $\tau_1 = \tau_2 = 0.25T$. Other parameters as in Fig. 2(a).

and the ghost of another. In other words the emission of the second pulse coincides with the backpropagation of the first pulse through the gain. This is also the reason why the HML₂ and HML₄ solutions do not restabilize in Fig. 3(a). However, restabilization can be obtained for asymmetrical cavity configurations, which will be discussed further.

We now turn our attention to the pulse clusters observed in Fig. 2. The bifurcation diagram of the PC₂ and PC₃ solutions is shown in Fig. 4 for an intermediate cavity length ($\gamma_g T = 9.4$). We note that, although the clusters are composed of nonequidistant pulses—see Figs. 4(b₁₋₂)—their separation is such that, considering the additional ghost pulses due to nonlocal effects, they induce equispaced carrier gain depletions. One understands that this leads to the larger gain extraction and to the more energetically favorable situation. In addition, it is also possible to find

“irregular” pulse cluster solutions, as indicated by the PC_4 irreg solution in Fig. 4(b₃). In order to understand these “irregular” regimes, one simply has to make a permutation between a real pulse and its ghost, thereby generating the same temporal profile for the gain dynamics. A similar irregular regime can be found for the PC_3 cluster. The PC states are multistable below the threshold in the same regions as the harmonic mode-locking solutions, as discussed before in Fig. 3(a). Equally, they stabilize in torus bifurcations [tr labeled circles in Fig. 4(a)] slightly above the SN point, i.e., the lower existence boundary. Following the PC_2 solution down to small pulse intensities, we find that it is born in a period doubling (PD) bifurcation of the HML_2 solution. Along the solution branch the two pulses of the PC_2 adjust their relative temporal distance from $\Delta_{PC_2} = 0.5T$ at the PD point (an enlargement of this region is given in Fig. 10 in Appendix D) to $\Delta_{PC_2} = 0.25T$ (PC_2) in the stable regime. It has to be noted that the generation mechanism of the PC solutions is different from that observed in the nonlocalized mode-locking regime. In the latter, additional pulses continuously emerge, increasing the bias along the FML solution branch [33].

The position of a solitary pulse in a PC is always limited by the two surrounding gain depletions; see, e.g., Fig. 2(d). We can assess the nature of this bond in dependence of the cavity round-trip time by performing a Floquet analysis [62] of the periodic PC_n solutions as described in Ref. [25]. In particular, for intermediate round-trip times where the gain does not relax to the equilibrium value, only one neutral mode exists for the pulse cluster in the cavity (see Fig. 9 in Appendix C), i.e., one Floquet multiplier is located at $\mu = 1$. This multiplier corresponds to the neutral mode of translation of the entire waveform. It is present in any dynamical system without explicit time dependence. As a counterexample, this multiplier would disappear in the analysis of an actively mode-locked laser because the pulse timing is locked to that of the externally imposed modulation. In our case, as the round-trip time is increased, $n - 1$ additional Floquet multipliers approach $\mu = 1$, where n is the number of pulses in the PC solution. As the gain fully relaxes in-between pulses, n Floquet multipliers at $\mu = 1$ can be found, as shown for the PC_2 solution in Fig. 9 in Appendix C. Hence, there is one neutral mode of translation for each pulse in one cluster, which demonstrates that they are locally independent. Notwithstanding, they remain globally bound since, for each pulse, the previous and next gain depletions induce repulsive forces. These incoherent molecules are similar to the nested molecules found in Ref. [25]. As the Floquet exponents give a measure of the residual interaction of the pulses, one can note that the transition between locally independent molecules and bound states is continuous depending on the round-trip time [see the exponential behavior in Fig. 9(f) in Appendix C].

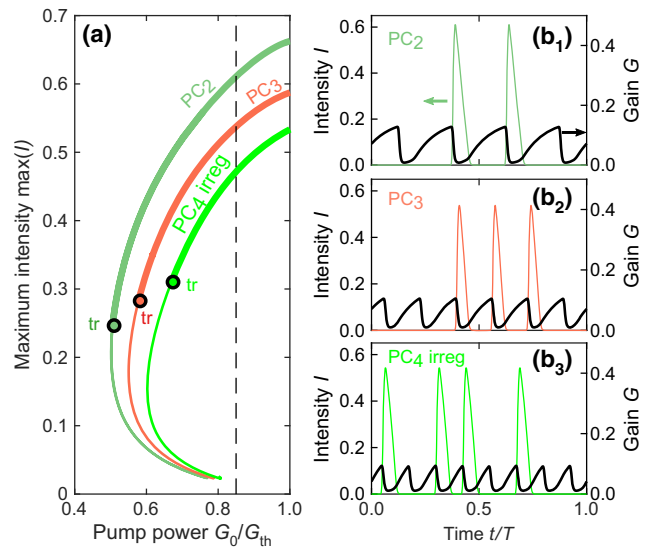


FIG. 4. (a) Maximum pulse intensity of bound PC states with different numbers of pulses with respect to the normalized pump power G_0/G_{th} . Thick and thin lines indicate stable and unstable solutions, respectively. The branches of the PC solutions with two and three pulses (PC_2 and PC_3) as well as the irregular four pulses solution (PC_4 irreg) all become stable below the threshold G_{th} . The stabilizing torus bifurcations (tr) are marked by black circles. The corresponding electric field intensity and gain profiles in the stable regions at $G_0 = 0.85G_{th}$ (dashed line) are displayed in (b₁₋₃). The PC solutions are shown for a symmetric cavity $\tau_2 = 0.25T$; all other parameters are as given in Fig. 2(a).

In order to investigate the effect of the cavity geometry on the existence of different localized multipulse states, we explore how the stabilizing torus and SN bifurcations of the FML and HML solutions in Fig. 3(a) change as a function of the pump power and of the cavity asymmetry. By introducing the condition $2\tau_1 + 2\tau_2 = T$ we keep the cavity round-trip time T constant, while changing the cavity geometry. The resulting SN and tr lines in the $(G_0/G_{th}, \tau_2/T)$ plane are shown in Figs. 5(a₁₋₂), respectively. Both bifurcations clearly show a resonance behavior with respect to the position of the gain chip τ_2 . For certain cavity configurations, no stabilizing torus bifurcation can be found and the curves in Fig. 5(a₂) are discontinuous; at these parameter values, two pulses collide in the gain chip as the distance between the pulses equals the propagation time between the two gain passes (e.g., $2\tau_2 = 0.5T$ for HML_2 or $2\tau_2 = 0.33T$ for HML_3). Hence, the number of resonances equals the number of pulses in the corresponding HML solution. This behavior can also be noted in Fig. 3(a) as there is no stable region for the even HML_2 and HML_4 states at $\tau_2 = 0.25T$.

Oppositely, resonances at which the stabilizing torus and lower saddle node reach the lowest pump power can be found in Figs. 5(a₁₋₂). They correspond to the cavity configurations at which the maximum gain saturation

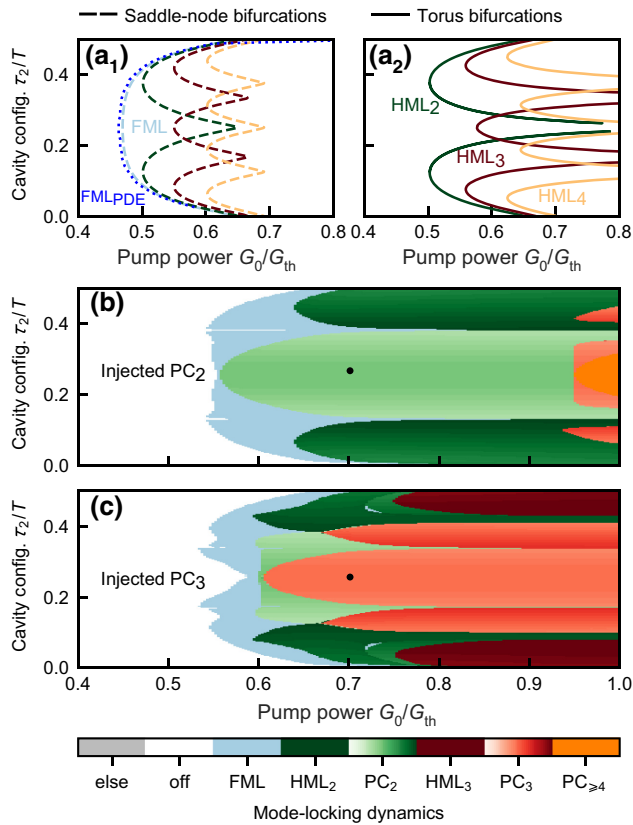


FIG. 5. (a₁) Saddle-node (folding) and (a₂) torus (stabilizing) bifurcations in the (G_0, τ_2) plane; the colors indicate FML, HML, and PC dynamics. Subscripts label the number of pulses in the cavity, $\alpha_{g,q} = 0$. For comparison, the numerically found saddle-node line of the FML solution resulting from the PDE model is plotted in dark blue in (a₁). (b),(c) Stable localized pulsations, evolving after injecting different PC solutions into the empty cavity as initial conditions (stable at the filled black circles). The injected solutions are found to be stable after 10^4 round trips at $G_0 = 0.7G_{\text{th}}$. The injected solutions are (b) PC₂ and (c) PC₃. The color coding is such that the pulse distance Δ_{PC_n} increases for darker shading with a separation of $0.5T$ at the maximum. Here $(\alpha_g, \alpha_q) = (1.5, 0.5)$; all other parameters are as given in Fig. 2(a).

can be achieved due to the pulses passes happening at the largest temporal interval. Maximizing gain extraction further explains why, in a symmetric cavity, the PC₂ solution is stable while the HML₂ is not [cf. Figs. 3(b₂) and 4(b₁)]; the former induces four gain depletion while the latter creates only two.

In order to obtain an overview of the stable regions of the PC states, we inject a PC solution found at a symmetric cavity configuration with $G_0 = 0.7G_{\text{th}}$ —see the filled circles in Figs. 5(b) and 5(c)—and record to which solution the system converges after an integration time of 10^4 round trips. This analysis is performed in the $(G_0/G_{\text{th}}, \tau_2/T)$ plane. We set $(\alpha_g, \alpha_q) = (1.5, 0.5)$ to better

match previous works [4,60,63]. Our results are shown in Figs. 5(b) and 5(c). The color code distinguishes the localized solution to which the system relaxes after a transitory regime.

To ensure optimal gain depletions, the pulse distances in the PC solutions are additional degrees of freedom by which these states can adapt to changes in the length of the cavity arms. The variation of the pulse distances in the stabilized PC solution is encoded in the shading of the colors indicating PC₂ and PC₃ solutions in Figs. 5(b) and 5(c), with ascending pulse distance from bright to dark colors. If the cavity is shifted slightly away from a symmetric positioning, say $\tau_2 = 0.25T$ in Figs. 5(b) and 5(c) for the PC₂ solution, the distance decreases to adjust for an optimal gain depletion. When the gain chip is placed at one of the edges of the cavity, top and bottom in Figs. 5(b) and 5(c), a solution with (almost) equally spaced pulses stabilizes. Hence, incoherent photonic molecules with specific pulse distances can be designed by adequately tuning the cavity geometry.

III. NONLOCAL HAUS MASTER EQUATION

In order to understand the relationship between pulse distances and cavity configuration, we derive a Haus master equation model for the investigated V-shaped laser system (1)–(4). Using a decomposition of the dynamics in slow and fast stages, we can obtain an analytical expression for the pulse distance and the pulse power as a function of τ_1, τ_2 .

We start the derivation of a Haus master equation model [64] from the DDEs (1)–(4) describing the V-shaped cavity system. The resulting partial differential equation (PDE) system could potentially also be used to study dispersive effects and spatiotemporal instabilities [30,31,65]. Although it is possible to investigate dispersion effects using a DDE approach [66,67], it is a more demanding and less intuitive approach. The details of the derivation of the master equation model are given in Appendix E; the derivation is based on the multitimescale analysis presented in Ref. [68], but can in principle also be done utilizing the functional mapping approach outlined in Refs. [69,70]. For the multitimescale analysis, we introduce the slow timescale θ corresponding to the electric field evolution from round trip to round trip and the fast timescale σ describing the pulse shape within one round trip [4,71]. Furthermore, we assume the limit of small gain G , which is fulfilled in the subthreshold regime as $G_{\text{th}} = 0.18$ for the chosen parameters and also the absorption is small as $Q_0 = 0.18$. Hence, we are investigating the system in the so-called uniform field limit, which refers to the gain, absorption, losses ($1 - \kappa = 0.01$), and spectral filtering being small. The full PDE system

then reads

$$\partial_\theta E = \frac{1}{2\gamma^2} \partial_\sigma^2 E + \left\{ \frac{1}{2} (1 - i\alpha_g) \left[G \left(\sigma - \frac{T - 2\tau_2}{T} \right) + G \right] - (1 - i\alpha_q) Q + \frac{1}{2} \log(\kappa) \right\} E, \quad (5)$$

$$\partial_\sigma G = \gamma_g G_0 - \gamma_g G - G \left[|E|^2 + \left| E \left(\sigma - \frac{2\tau_2}{T} \right) \right|^2 \right], \quad (6)$$

$$\partial_\sigma Q = \gamma_q Q_0 - \gamma_q Q - 2sQ|E|^2, \quad (7)$$

where all parameters have the same meaning as in the DDE system (1)–(4) in Sec. II. The natural boundary condition is the asynchronous boundary condition $G(\theta + 1, 0) = G(\theta, L)$, where L is the length of the cavity. This way the history of the carrier dynamics evolution is also taken into account. Yet, for perfectly localized states, the gain would completely recover to the equilibrium value in-between two depletions, i.e., $G(\theta + 1, 0) = G_0$, which is exploited for the path continuation. When investigating cavity lengths in the intermediate regime in contrast, a more sophisticated boundary condition is necessary for the path continuation and numerical integration [72]. For numerical simulations of the system (5)–(7), we utilize the Fourier split step method as outlined in Appendix 4 of Ref. [31].

The two nonlocal terms in the electric field and the gain equation describe the influence of the cavity geometry. Each pulse experiences a second amplification on its way back through the cavity at $T - 2\tau_2 = 2\tau_1$ and, hence, the gain is depleted twice during one round trip of a single pulse.

Utilizing the path continuation package pde2path [73], we can reconstruct the branches of both FML and PC solutions and find good agreement with the previously presented DDE results, as clearly shown for the FML branch in Fig. 3(a) (dark blue line). Finding this agreement is also possible when varying the α factors. Furthermore, the lower stability boundary of the FML solution (SN bifurcation) can be reproduced very well by the nonlocal Haus master equations (5)–(7), as indicated by the dark blue dotted line in Fig. 5(a₁), which is almost identical to the result obtained from the DDE model (1)–(4).

Note that in addition to the standard Haus model [64], the nonlocal model (5)–(7) makes it possible to study the effects of the cavity geometry combined with the advantages of including dispersion and transverse diffraction effects. A thorough analysis of the differences in the bifurcation structure of the local and nonlocal Haus models is still subject to further investigation, but several alterations can be expected as the first principle DDEs, from which the Haus models can be derived, already differ in the stabilizing bifurcations of, e.g., HML_{*n*} branches (e.g., tr bifurcation instead of SN [3]; cf. Fig. 3). The fundamental branches in both local and nonlocal cases however

appear to be very similar [60]. Furthermore, we expect differences especially when tuning the value of α_g , due to the additional nonlocality in the electric field, Eq. (5).

IV. BOUND PULSE DISTANCES

Utilizing the nonlocal Haus master equations (5)–(7), we can derive an analytic expression predicting how the pulse distance Δ_{PC_n} in regular pulse clusters [see, e.g., Figs. 4(d_{1–2})] changes with the cavity configuration and how the resulting pulse power depends on the pump power at different cavity configurations. A detailed derivation of the resulting equations for the PC₂ solution can be found in Appendix F.

We start by decomposing the gain and absorber dynamics into slow and fast stages and assume a neglectable pulse width ε . The fast stage in which the gain or absorber is depleted by the pulse can be approximated by $G_f^{(n)} = G_i^{(n)} e^{-P_n}$, where $G_f^{(n)}$ is the gain value after the pass of pulse n , $G_i^{(n)}$ is the gain value just before the incidence of the pulse, and P_n is the n th pulse power. On the slow timescale we approximate the gain relaxation by

$$G_i^{(n+1)} = G_f^{(n)} e^{-\gamma_g \Delta} + G_0 [1 - e^{-\gamma_g \Delta}], \quad (8)$$

where Δ is the distance between the pulses and $G_i^{(n+1)}$ is the initial gain value prior to pulse $n + 1$. A full set of resulting equations for the decomposition of the gain and absorber dynamics, including all depletions, can be found in Appendix F. In order to be able to solve the system of algebraic equations for Δ , we utilize the extra condition that all pulses are identical, i.e., they experience the same effective gain. Hence, we can recover a relation connecting the pulse energy $P_n = P$ and the distance between the pulses of the PC solution Δ . As the resulting equation is highly singular, a prediction for the pulse distances can be deduced from physical arguments (real and non-negative pulse powers—see Fig. 12 in Appendix F for details). This procedure can also be applied for higher-order PC solutions. In particular, for the PC₂ and PC₃ solutions, the relations read

$$\Delta_{\text{PC}_2} = \frac{T - 2\tau_2}{2} - \frac{1}{2\gamma_g} \log \left(\frac{1 + e^{\gamma_g (T - 4\tau_2)}}{2} \right), \quad (9)$$

$$\Delta_{\text{PC}_3} = \frac{T - 2\tau_2}{3} - \frac{1}{3\gamma_g} \log \left(\frac{1 + e^{\gamma_g (T - 4\tau_2)}}{2} \right). \quad (10)$$

Both distances are only dependent on the cold cavity round-trip time T , the gain relaxation γ_g , and the configuration of the cavity given by τ_2 . Utilizing path continuation for the DDE (or PDE) system, we obtain the solution branches of the PC₂ (PC₃) solution in τ_2 (keeping T constant) and determine the pulse distances along the solutions. The result is shown in Fig. 6(a), with the

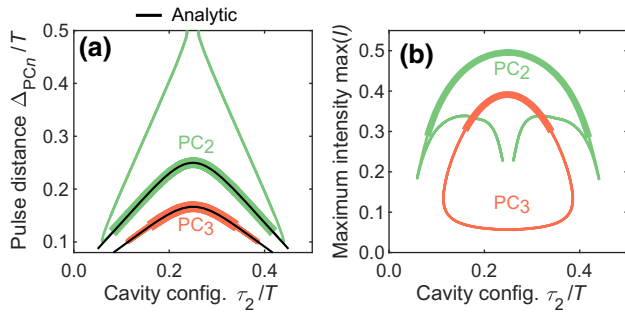


FIG. 6. (a) Change of the pulse distances Δ_{PC_n} within the PC_2 (green) and PC_3 (red) solutions for varied cavity configurations τ_2 calculated utilizing path continuation of the DDEs (1)–(4) and the analytical expressions (9) and (10) (black lines). Thick lines indicate stable regions; thin lines correspond to unstable solutions. (b) Maximum pulse intensity along the branch shown in (a). Here $G_0/G_{th} = 0.67$; all other parameters are as given in Fig. 2(a).

path continuation result in green (red) and the respective analytic expressions (9) and (10) in black.

The analytic expressions (9) and (10) accurately match the path continuation results in the stable regimes, which are depicted by thick lines (thin colored lines indicate unstable solutions). At the outer ends of the stable regimes ($\tau_2 \approx 0.05T$ and $\tau_2 \approx 0.45T$), the PC_2 solution branch loops back and the pulse distance grows until the branch reconnects with the HML_2 solution at $\tau_2 \approx 0.25T$ [open ends in Fig. 6(b)]. On the contrary, the PC_3 solution is a closed loop and reconnects to itself, as shown in Fig. 6(b), and the pulse distances are equal for the stable and unstable regimes. Nevertheless, the amplitudes of stable and unstable solutions are different and drop significantly for the unstable solution [Fig. 6(b)]. This can be explained by the corresponding gain dynamics, which is optimal if the average gain is kept as low as possible (large depletions). In the case of the PC_2 solution, an unstable regime near the symmetric cavity configuration exists in which the pulses come close to the HML_2 branch [top of Fig. 6(a)]. Here the pulses deplete the gain simultaneously ($\Delta_{PC_2} \rightarrow 0.5T$), which is energetically less favorable and therefore leads to the dynamics being unstable.

V. CONCLUSION

Investigating a passively mode-locked laser with V-shaped external cavity geometry in the long cavity limit, we find that temporal localized structures can be excited individually below the lasing threshold. Because of the V-shaped cavity configuration, in which the gain is depleted twice during each round trip, phase incoherent molecules can also be stabilized. The latter emerge as clusters of closely packed (incoherent) pulses. Performing a Floquet analysis, we show that the pulses within a cluster are globally bound yet locally independent if the cavity is

long enough and highlight that this is a consequence of the nonlocal interaction with the carriers. Applying path continuation and direct numerical integration techniques, we predict the stability boundaries of harmonic and pulse cluster solutions with respect to the cavity configuration. This reveals that the stabilization of both types of dynamics is mainly influenced by the maximization of the gain depletion.

We derive a nonlocal master equation to better understand the nonlocal influence of the double gain depletion in the V-shaped cavity. Utilizing this nonlocal PDE system, analytical expressions predicting the pulse power with respect to the gain and most importantly the pulse distance within one cluster with respect to the gain recovery time and the cavity configuration are obtained. In conclusion, we provide a theoretical framework to tailor the energy and pulse distance in bound pulse clusters in the intermediate and localized regime and facilitate their experimental observation. Our findings can have both fundamental and practical interests with regard to the generation of controlled pulse patterns from a single mode-locked laser or the circumvention of unwanted regimes. The bound pulse patterns could find applications in optical communications, e.g., to implement new bit encoding or at higher powers for material processing. Because of their dense frequency combs, the found clusters could also be utilized in spectroscopy applications requiring a careful distribution of the comb power across several pulses and the timing of arrival at the sample.

ACKNOWLEDGMENTS

J.H., S.M., and K.L. thank the Deutsche Forschungsgemeinschaft (DFG) within the frame of the SFB787 and the SFB910 for funding. J.J. acknowledges financial support from the MINECO Project MOVELIGHT (PGC2018-099637-B-100 AEI/FEDER UE). S.G. acknowledges the PRIME program of the German Academic Exchange Service (DAAD) with funds from the German Federal Ministry of Education and Research (BMBF).

APPENDIX A: COORDINATE TRANSFORMATION

In order to give a better insight into the dynamics induced by the cavity geometry, we illustrate the interaction of the electric field and the active sections during one round trip utilizing the DDE system in which the time is not transformed for computational reasons. As presented in Ref. [33], this system reads

$$\begin{aligned} \frac{dE(t')}{dt'} &= -\gamma E(t') + \gamma \sqrt{\kappa} E(t' - 2\tau_2 - 2\tau_1) \\ &\times e^{[(1-i\alpha_g)/2][\tilde{G}(t' - \tau_1 - 2\tau_2) + \tilde{G}(t' - \tau_1)]} \\ &\times e^{(1-i\alpha_q)\tilde{Q}(t' - \tau_1 - \tau_2)}, \end{aligned} \quad (\text{A1})$$

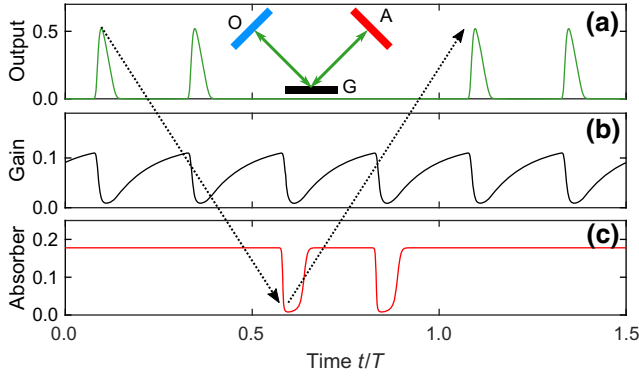


FIG. 7. Electric field (green) at the output, gain (G in black) and absorber (A in red) dynamics in the untransformed DDE model. The arrow indicates the interaction of the pulse with the active sections during one round-trip, starting and ending at the output coupler (O).

$$\frac{d\tilde{G}(t')}{dt'} = J_g - \gamma_g \tilde{G}(t') - (e^{\tilde{G}(t')} - 1) \{|E(t' - \tau_1)|^2 + |E(t' - \tau_1 - 2\tau_2)|^2 e^{2\tilde{Q}(t' - \tau_2) + \tilde{G}(t' - 2\tau_2)}\}, \quad (\text{A2})$$

$$\frac{d\tilde{Q}(t')}{dt'} = J_q - \gamma_q \tilde{Q}(t') - r_s (e^{2\tilde{Q}(t')} - 1) e^{\tilde{G}(t' - \tau_2)} |E(t' - \tau_1 - \tau_2)|^2, \quad (\text{A3})$$

and has several additional delayed terms. The consecutive interaction of a pulse cluster with the active sections in the V-shaped cavity is indicated in Fig. 7. Starting at the outcoupling facet, each pulse first depletes the gain after a time τ_1 (first intersection of the dotted arrow with the gain), which is given by the $\tilde{G}(t' - \tau_1 - 2\tau_2)$ term in Eq. (A1). Hereinafter the pulse depletes the absorber after a time $\tau_1 + \tau_2$ [$\tilde{Q}(t' - \tau_1 - \tau_2)$] and then again the gain at $\tau_1 + 2\tau_2$ given by the term $\tilde{G}(t' - \tau_1)$ (second intersection of the dotted arrow with the gain). The pulse cluster results from the equal gain passages, which are energetically favorable.

In order to reduce the number of delays to improve the computational costs, we introduce the coordinate transformation $t' = t + \tau_1$ for Eq. (A2) and $t' = t + \tau_1 + \tau_2$ for Eq. (A3). We further redefine the variables according to:

$$\tilde{G}(t + \tau_1) = G(t), \quad \tilde{Q}(t + \tau_1 + \tau_2) = Q(t), \quad (\text{A4})$$

leading to the model presented in Eqs. (1)–(4).

APPENDIX B: ELECTRICAL TRIGGERING OF LSs

As demonstrated experimentally with face-to-face coupled cavities [4,6], localized pulses can be triggered via

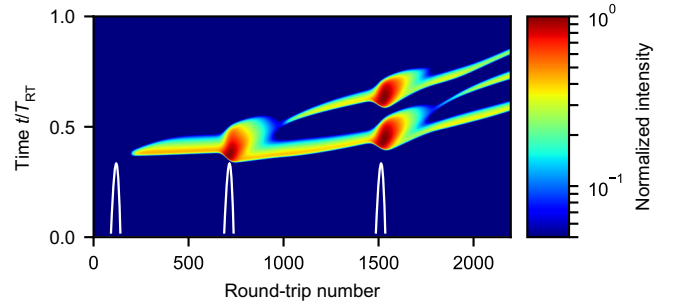


FIG. 8. Space-time representation of pulse trains that are excited below the threshold G_{th} . The y axis corresponds to the fast timescale normalized to one period of the fundamental solution (T_{RT}) and the x axis to the evolution over several periods (round trips in the cavity). Additional pulses can be written by applying a Gaussian-shaped pump pulse to the constant pump $G_0 = 0.85G_{\text{th}}$. The amplitudes and FWHMs of the first two and third excitations are $\Delta G_0 = 2.2G_{\text{th}}$, $T_{\text{FWHM}} = 47T$ and $\Delta G_0 = 2.75G_{\text{th}}$, $T_{\text{FWHM}} = 59T$, respectively. Here $\tau_2 = 0.15$ with all other parameters as given in the text. The Gaussian pulse is centered at 100, 700, and 1500 round trips, indicated by the white lines.

electrical excitation. This can be experimentally achieved by either applying a periodic current modulation [4], by starting the laser above threshold and then sweeping down the pump current [3], or by applying single electrical pulses [4]. The resulting dynamics from a numerical investigation of the latter excitation scheme is shown in a pseudo-space-time diagram [74] in Fig. 8. Here, the y axis corresponds to the fast timescale, i.e., changes of the electric field within one round trip, and the x axis refers to the evolution from one round trip to the next. For the electric excitation, a Gaussian-shaped pump pulse is superimposed to the constant pump current ($G_0 = 0.85G_{\text{th}}$). Three electrical pulses are subsequently applied to the system with a short intermediate transient time; cf. the white lines in Fig. 8. The amplitudes are $\Delta G_0 = 2.2G_{\text{th}}$ for the first two excitation pulses and $\Delta G_0 = 2.75G_{\text{th}}$ for the third. As can be seen in Fig. 8, the first perturbation of the lasing system in the “off” state creates a single localized pulse. Additional pulses can be generated when applying further electrical pulses, as indicated by the second and third excitation. However, in contrast to the case of a face-to-face coupled cavity [3,4,6], the additional pulse does not stabilize to a harmonic mode-locking solution corresponding to an equidistant pulse spacing. Contrarily, the pulses relax to a state in which they are bound in a cluster by the nonlocal influence of the second gain depletion within one round trip, resulting from the V-shaped cavity configuration.

APPENDIX C: FLOQUET ANALYSIS

The Floquet multipliers [62] give rise to a further classification of how the pulses in one cluster are bound [25].

They result from the linear stability analysis of the periodic PC solutions of the system. If the absolute value of all Floquet multipliers μ is less than 1, the solution is considered to be stable. One (trivial) Floquet multiplier can always be found at $\mu = 1$. It corresponds to the neutral mode of the system, when perturbed in the direction that corresponds to a translation of the time origin.

Considering the PC₂ solution at high round-trip times, the gain relaxes to its equilibrium value in-between pulses. Therefore, the pulses are locally independent, but globally bound by the depletions induced by the neighboring pulse, as shown in Fig. 9(e). This is supported by the Floquet multipliers, as two neutral modes can be found for this type of pulse cluster, i.e., two Floquet multipliers at $\mu = 1$, marked by the green and red circles in Fig. 9(a). The corresponding two eigenvectors also refer to the relative

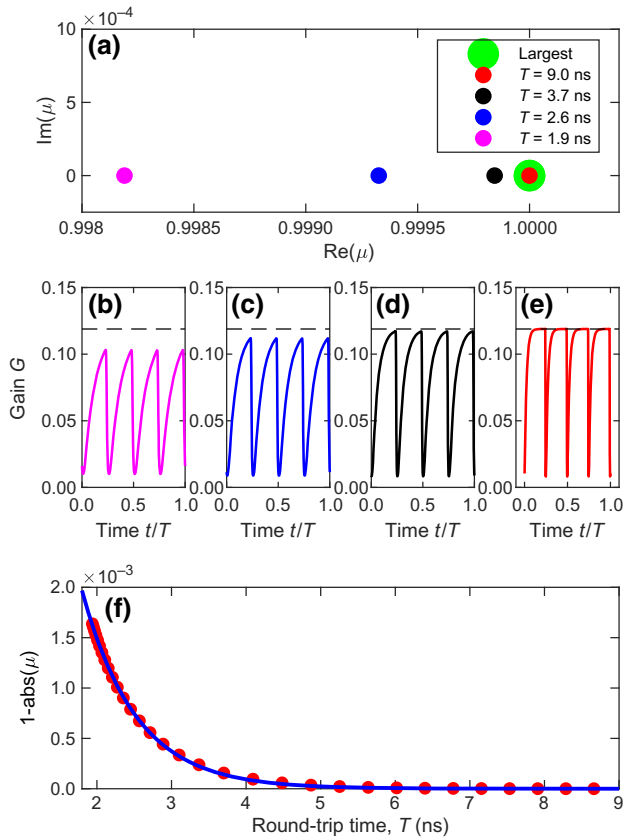


FIG. 9. (a) Real and imaginary parts of the two maximum Floquet multipliers μ of the PC₂ solution at different round-trip times (denoted by colors). At each T , the maximum Floquet multiplier is located at $\mu = 1$, indicated by the large green circle. The second largest Floquet multiplier comes closer to $\mu = 1$ as the round-trip time is increased. The corresponding gain dynamics is shown in (b)–(e), with the equilibrium value indicated by the dashed line. (f) Distance of the absolute value of the second largest Floquet multiplier to unity at different round trips found using DDE-Biftool (red) and exponential fit (blue). Parameters as in Fig. 2 and $G_0/G_{\text{th}} = 0.65$.

temporal translation of either of the two localized states. As the round-trip time is decreased, the gain is not able to relax in-between pulse passes, as shown in Figs. 9(b)–9(d), with the equilibrium value indicated by the dashed black line. In this case the second largest Floquet multiplier becomes smaller than unity and therefore the pulses are also locally bound at low T , because there is no second neutral mode [see the magenta circle in Fig. 9(a)]. This behavior can also be found for higher-order pulse clusters in which the number of neutral modes equals the number of pulses in the cluster, if T is sufficiently high. As the second largest Floquet exponent exponentially approaches unity [shown in Fig. 9(f)], we also conclude that the transition between locally independent molecules and bound states is continuous depending on the round-trip time.

APPENDIX D: EVOLUTION OF THE PC₂ SOLUTION

The localized bound PC₂ solution is born unstable in a period doubling (PD) bifurcation along the HML₂ branch, as indicated by the blue diamond in Fig. 10(a). As expected, the solution is very similar to the HML₂ solution close to the bifurcation point [Fig. 10(b₁)]. However, along the branch the intensity of both pulses subsequently drops [Fig. 10(b₂)] to a minimum and, as they recover, the pulse distance shrinks to $\Delta_{\text{PC}_2} = 0.25T$ for $\tau_2 = 0.25T$ [Fig. 10(b₃)] until the pulse cluster regime stabilizes in a torus (tr) bifurcation with corresponding electric field dynamics in Fig. 10(b₄).

As described in the main text, only two gain depletions can be found for the HML₂ solution in the symmetric

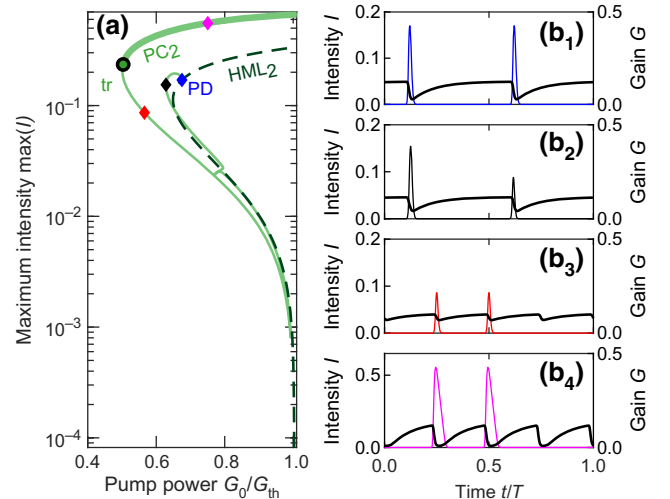


FIG. 10. Evolution of the PC₂ solution born in a period doubling bifurcation (PD) of the HML₂ branch and then stabilizing in a torus bifurcation (tr). (a) Solution branches continued in G_0 of the PC₂ and HML₂ solutions. (b₁–4) Gain and electric field profiles at the points of the branch marked by the colored diamond.

cavity configuration chosen in Fig. 10(b₁), as the pulse distance $\Delta_{\text{HML}_2} = 0.5T$ equals $2\tau_2 = 0.5T$, i.e., two pulses deplete the gain simultaneously. This changes as the pulses come closer to each other in Figs. 10(b₃₋₄) and deplete the gain at a maximum temporal separation.

APPENDIX E: DERIVATION OF THE NONLOCAL HAUS EQUATION

The derivation is based on the multitimescale approach presented in Ref. [68]. We start the derivation with the DDE model (1)–(4) for the passively mode-locked laser with V-shaped cavity geometry derived in Ref. [33], but rescale the time by one round trip $t = \tilde{t}/T$. The field is rescaled so that $A = E\gamma_g^{-1}$ and $\tilde{s} = s(\gamma_g/\gamma_q)$. In contrast to the model equations shown in Ref. [33] all other parameters are not rescaled to the round-trip time at this point. As the localized structures are found in the subthreshold regime, we can assume small gain and absorption. We introduce the smallness parameter $\varepsilon = \gamma^{-1}T^{-1}$, which is proportional to the pulse width and rescale the variables and parameters according to

$$\tilde{G} = \varepsilon^2 G, \quad \tilde{Q} = \varepsilon^2 Q, \quad (\text{E1})$$

$$G_0 = \varepsilon^2 G_m, \quad Q_0 = \varepsilon^2 Q_m, \quad (\text{E2})$$

$$\kappa = \exp(-\varepsilon^2 k). \quad (\text{E3})$$

One should note that $\gamma_g T$ is not of the order of ε^2 (in contrast to the short cavity case in Ref. [68]), as we investigate the localized regime in which $\gamma_g T > 1$ is a necessary condition. Therefore, $\gamma_g T$ and $\gamma_q T$ are not rescaled.

Inserting the rescaled variables and parameters and expanding for ε leads to

$$\begin{aligned} \varepsilon \frac{dA}{dt} = & -A + A(t-1) \left\{ 1 + \frac{\varepsilon^2}{2} \left[G \left(t - \frac{2\tau_1}{T} \right) \right. \right. \\ & \left. \left. + G(t-1) - 2Q(t-1) - k \right] \right\} + O(\varepsilon^4), \end{aligned} \quad (\text{E4})$$

$$\frac{dG}{dt} = \gamma_g T \left[G_m - G - G \left\{ |A|^2 + \left| A \left(t - \frac{2\tau_2}{T} \right) \right|^2 \right\} \right] + O(\varepsilon^2), \quad (\text{E5})$$

$$\frac{dQ}{dt} = \gamma_q T [Q_m - Q - 2\tilde{s}Q|A|^2] + O(\varepsilon^2). \quad (\text{E6})$$

We can now introduce a fast timescale σ and a slow timescale θ . However, we allow the period to vary on the fast timescale, which is similar to applying the Poincaré-Linstedt method. Hence, we define the new timescales as

$$\sigma = (1 + \omega_1 \varepsilon + \omega_2 \varepsilon^2)t, \quad (\text{E7})$$

$$\theta = \varepsilon^2 t, \quad (\text{E8})$$

where the ω_j will be chosen to make the solvability conditions as simple as possible. Choosing $\mathcal{O}(\varepsilon^2)$ for the slow timescale is motivated by the timescale of amplitude (gain) fluctuations and the fast timescale includes period-1 oscillations and the drift resulting from the time lag induced by the spectral filter [71]. The drift can physically be understood by the fact that the period of one pulse train in the LS regime ($T_{\text{per}} \approx T + \gamma^{-1}$) will always be larger than the cold cavity round-trip time T , due to causality. Therefore, the total derivative d/dt becomes

$$\frac{d}{dt} \Rightarrow (1 + \omega_1 \varepsilon + \omega_2 \varepsilon^2) \partial_\sigma + \varepsilon^2 \partial_\theta. \quad (\text{E9})$$

Hence, we find, for the delayed terms,

$$\begin{aligned} & A(\sigma - 1 - \omega_1 \varepsilon - \omega_2 \varepsilon^2, \theta - \varepsilon^2) \\ &= A(\sigma - 1, \theta) - (\varepsilon \omega_1 + \varepsilon^2 \omega_2) \partial_\sigma A(\sigma - 1, \theta) \\ &\quad - \varepsilon^2 [\partial_\theta A(\sigma - 1, \theta) + \omega_1^2 \partial_\sigma^2 A(\sigma - 1, \theta)] + O(\varepsilon^3). \end{aligned} \quad (\text{E10})$$

We are searching for a solution of the form $A(\sigma, \theta, \varepsilon)$, $G(\sigma, \theta, \varepsilon)$, and $Q(\sigma, \theta, \varepsilon)$; we approximate all variables as a power series in ε , i.e.,

$$A(\sigma, \theta, \varepsilon) = A_0(\theta, \sigma) + \varepsilon A_1(\theta, \sigma) + \varepsilon^2 A_2(\theta, \sigma), \quad (\text{E11})$$

and find the equations for the $\mathcal{O}(1)$, $\mathcal{O}(\varepsilon)$, and $\mathcal{O}(\varepsilon^2)$ problems. Using $A(\sigma, \theta) \hat{=} A$ and $A(\sigma - 1, \theta) \hat{=} A(\sigma - 1)$ for simplicity, we obtain, for $\mathcal{O}(1)$,

$$A_0 = A_0(\sigma - 1), \quad (\text{E12})$$

$$\partial_\sigma G_0 = \gamma_g T \left[G_m - G_0 - G_0 \left\{ |A_0|^2 + \left| A_0 \left(\sigma - \frac{2\tau_2}{T} \right) \right|^2 \right\} \right], \quad (\text{E13})$$

$$\partial_\sigma Q_0 = \gamma_q T [Q_m - Q_0 - 2\tilde{s}Q_0|A_0|^2]. \quad (\text{E14})$$

Note that we have neglected the expansion in θ of the delayed term in (E13), as it is of order ε^2 . The same is true for the derivative of G_0 and Q_0 with respect to the slow timescale θ . From Eq. (E12) we can see that A_0 is of period 1.

We continue to go to higher order for the electric field and find $\mathcal{O}(\varepsilon)$:

$$\begin{aligned} & A_1 - A_1(\sigma - 1) = -\omega_1 \partial_\sigma A_0(\sigma - 1) - \partial_\sigma A_0, \\ \Rightarrow & A_1 - A_1(\sigma - 1) = -(1 + \omega_1) \partial_\sigma A_0. \end{aligned} \quad (\text{E15})$$

As the $(1 + \omega_1)$ term would introduce a resonant forcing, i.e., divergence, we require it to be 0 so that A_1 is also period 1. Therefore, solvability gives $\omega_1 = -1$.

For $\mathcal{O}(\varepsilon^2)$, we obtain

$$\begin{aligned}
 A_2 - A_2(\sigma - 1) &= -\omega_1 \partial_\sigma A_0 - \partial_\sigma A_1 - \partial_\theta A_0(\sigma - 1) \\
 &+ \frac{1}{2} \omega_1^2 \partial_\sigma^2 A_0(\sigma - 1) - \omega_2 \partial_\sigma A_0(\sigma - 1) \\
 &- \omega_1 \partial_\sigma A_1(\sigma - 1) \\
 &+ \frac{1}{2} \left[G_0 \left(\sigma - \frac{2\tau_1}{T} \right) + G_0(\sigma - 1) + 2Q_0(\sigma - 1) - k \right] \\
 A_0(\sigma - 1). & \tag{E16}
 \end{aligned}$$

Using the fact that A_0 and A_1 are 1 periodic, $\omega_1 = -1$, we find that $\omega_2 = 1$ with the same reasoning as before. Thus, we end up with the solvability condition

$$\begin{aligned}
 A_2 - A_2(\sigma - 1) &= -\partial_\theta A_0 + \frac{1}{2} \partial_\sigma^2 A_0 \\
 &+ \frac{1}{2} \left[G_0 \left(\sigma - \frac{2\tau_1}{T} \right) + G_0(\sigma - 1) + 2Q_0(\sigma - 1) - k \right] A_0.
 \end{aligned} \tag{E17}$$

Note that in the delayed G_0 terms the delay for the slow timescale is neglected as they are of order ε^2 in the expansion, which would give an order of ε^4 in total.

The final PDE system then reads

$$\begin{aligned}
 \partial_\theta A_0 &= \frac{1}{2} \partial_\sigma^2 A_0 + \frac{1}{2} \left[G_0 \left(\sigma - \frac{T - 2\tau_2}{T} \right) + G_0 - 2Q_0 - k \right] A_0, \\
 \partial_\sigma G_0 &= \gamma_g T \left[G_m - G_0 - G_0 \left\{ |A_0|^2 + \left| A_0 \left(\sigma - \frac{2\tau_2}{T} \right) \right|^2 \right\} \right], \\
 \partial_\sigma Q_0 &= \gamma_q T [Q_m - Q_0 - 2\tilde{s}Q_0 |A_0|^2].
 \end{aligned}$$

Rescaling γ_g into A , reinserting \tilde{s} , and reintroducing α_g, α_q finally yields

$$\begin{aligned}
 \partial_\theta A &= \frac{1}{2\gamma^2} \partial_\sigma^2 A + \left\{ \frac{1}{2} (1 - i\alpha_g) \left[G \left(\sigma - \frac{T - 2\tau_2}{T} \right) + G \right] \right. \\
 &\quad \left. - (1 - i\alpha_q) Q + \frac{1}{2} \log(\kappa) + i\omega \right\} A, \tag{E18}
 \end{aligned}$$

$$\begin{aligned}
 \partial_\sigma G &= \gamma_g G_m - \gamma_g G - G \left\{ |A|^2 + \left| A \left(\sigma - \frac{2\tau_2}{T} \right) \right|^2 \right\}, \\
 & \tag{E19}
 \end{aligned}$$

$$\partial_\sigma Q = \gamma_q Q_m - \gamma_q Q - 2sQ |A|^2. \tag{E20}$$

Please note that $Q_m = Q_0$ and $G_m = G_0$ in the main text and do not confuse it with the carrier decomposition.

APPENDIX F: CARRIER DECOMPOSITION

In order to find a relation connecting the pulse distance in a pulse cluster Δ_{PC_n} and the cavity configuration (T, τ_1, τ_2) , we decompose the gain and absorber dynamics into slow and fast stages. We find a sequence of equations for the gain $G_{kl}^{(n)}$ and absorber $Q_k^{(n)}$, where the subscript $k \in \{i, f\}$ refers to initial and final value of the gain or absorber (before and after the pass of the pulse) and (n) refers to the pulse number. The subscript $l \in \{1, 2\}$ of the gain variable indicates the first or second gain pass of pulse (n) in one round trip. The different points are displayed in Figs. 11(b) and 11(c). For the gain, we find the following sequence with pulse energy $P = \int_{-\varepsilon}^{+\varepsilon} |E|^2 d\sigma$, and pulse width ε :

$$t = -\varepsilon, \quad G_{i1}^{(1)}, \tag{F1}$$

$$t = +\varepsilon, \quad G_{f1}^{(1)} = G_{i1}^{(1)} e^{-P_1}, \tag{F2}$$

$$t = \Delta - \varepsilon, \quad G_{i1}^{(2)} = G_{f1}^{(1)} e^{-\gamma_g \Delta} + G_0 [1 - e^{-\gamma_g \Delta}], \tag{F3}$$

$$t = \Delta + \varepsilon, \quad G_{f1}^{(2)} = G_{i1}^{(2)} e^{-P_2}, \tag{F4}$$

$$\begin{aligned}
 t = 2\tau_2 - \varepsilon, \quad G_{i2}^{(1)} &= G_{f1}^{(2)} e^{-\gamma_g (2\tau_2 - \Delta)} \\
 &+ G_0 [1 - e^{-\gamma_g (2\tau_2 - \Delta)}], \tag{F5}
 \end{aligned}$$

$$t = 2\tau_2 + \varepsilon, \quad G_{f1}^{(2)} = G_{i2}^{(1)} e^{-P_1}, \tag{F6}$$

$$\begin{aligned}
 t = 2\tau_2 + \Delta - \varepsilon, \quad G_{i2}^{(2)} &= G_{f1}^{(2)} e^{-\gamma_g \Delta} \\
 &+ G_0 [1 - e^{-\gamma_g \Delta}], \tag{F7}
 \end{aligned}$$

$$t = 2\tau_2 + \Delta + \varepsilon, \quad G_{f2}^{(2)} = G_{i2}^{(2)} e^{-P_2}, \tag{F8}$$

$$\begin{aligned}
 t = T, \quad G_{i1}^{(1)} &= G_{f2}^{(2)} e^{-\gamma_g (T - 2\tau_2 - \Delta)} \\
 &+ G_0 [1 - e^{-\gamma_g (T - 2\tau_2 - \Delta)}]. \tag{F9}
 \end{aligned}$$

Because of the fast recovery rate of the absorber, it relaxes to the equilibrium Q_0 after each pulse. Furthermore, the absorber is passed only once per round trip. Therefore, the relations read

$$t = -\varepsilon, \quad Q_i^{(1)} = Q_0, \tag{F10}$$

$$t = +\varepsilon, \quad Q_f^{(1)} = Q_0 e^{-2sP_1}, \tag{F11}$$

$$t = \Delta - \varepsilon, \quad Q_i^{(2)} = Q_0, \tag{F12}$$

$$t = \Delta + \varepsilon, \quad Q_f^{(2)} = Q_0 e^{-2sP_2}. \tag{F13}$$

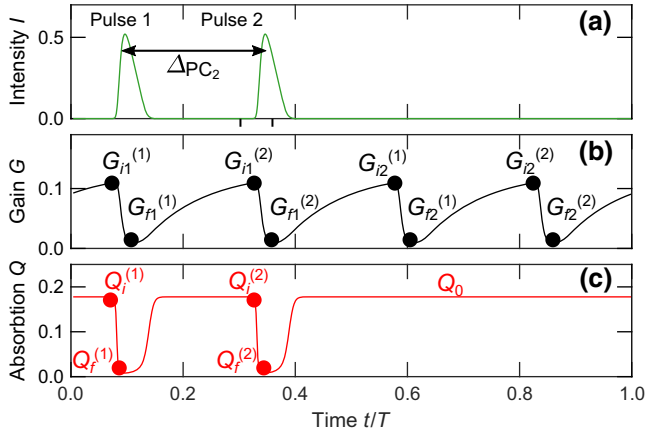


FIG. 11. (a) Intensity dynamics of the PC_2 solution. (b) Gain depletions of the PC_2 solution, with points described in Eqs. (F1)–(F9) marked by black circles. (c) Absorber dynamics, with points described by Eqs. (F10)–(F13) marked by red circles.

In order to solve the system of the equations for the gain, Eqs. (F1)–(F9) for Δ , we utilize the extra condition that the pulses in one cluster are equal, i.e., they experience the same effective gain:

$$G_{i1}^{(1)} + G_{i2}^{(1)} = \dots = G_{i1}^{(n)} + G_{i2}^{(n)}. \quad (\text{F14})$$

Solving the whole system then leads to the following relation between the pulse power P and the interpulse distance between the pulses Δ :

$$e^{2P} = \frac{2e^{\gamma_g \Delta} - e^{\gamma_g(2\tau_2 - \Delta)} - e^{\gamma_g(T - \Delta - 2\tau_2)}}{2e^{\gamma_g(T - \Delta)} - e^{\gamma_g(2\tau_2 + \Delta)} - e^{\gamma_g(T + \Delta - 2\tau_2)}}. \quad (\text{F15})$$

This is only negative, except for the location around the pole Δ_{PC_2} [see Fig. 12(a)]. Hence, the physical arguments restrict the solution to be at Δ_{PC_2} , where we find a positive value for e^{2P} and all values of the pulse energy are spanned rapidly. Thus, we can find a relation for the pulse distance, by solving for the pole:

$$2e^{\gamma_g(T - \Delta_{PC_2})} - e^{\gamma_g(2\tau_2 + \Delta_{PC_2})} - e^{\gamma_g(T + \Delta_{PC_2} - 2\tau_2)} = 0. \quad (\text{F16})$$

This simplifies to

$$\Delta_{PC_2} = \frac{T - 2\tau_2}{2} - \frac{1}{2\gamma_g} \log\left(\frac{1 + e^{\gamma_g(T - 4\tau_2)}}{2}\right). \quad (\text{F17})$$

The resulting dependence is visualized Fig. 12(b) for the PC_2 solution with the asymptotic for large and small τ_2

shown in orange. These read

$$\lim_{\tau_2 \rightarrow 0} \Delta_{PC_2} = \tau_2 + \frac{\log(2)}{2\gamma_g}, \quad (\text{F18})$$

$$\lim_{2\tau_2 \rightarrow T} \Delta_{PC_2} = \frac{T - 2\tau_2}{2} + \frac{\log(2)}{2\gamma_g}. \quad (\text{F19})$$

In order to also find an expression for the relationship between the pulse power and pump current, we further integrate Eq. (5) over each pulse n in the cluster at position σ_n . We assume that the pulse width ε is small and apply New's approximation [75], which is sufficient in the subcritical strongly nonlinear LS regime, if the out-coupling losses dominate. Furthermore, the pulse energy P does not change on the slow timescale in a steady state, i.e., $dP/d\theta = 0$. We find that the locus for the pulse existence is given by the zeros of the following integral for the various pulses:

$$\mathcal{I}_n = \int_{\sigma_n - \varepsilon}^{\sigma_n + \varepsilon} \left[\frac{1}{2} G(\sigma - 2\tau_1) + \frac{1}{2} G(\sigma) - Q(\sigma) + \frac{1}{2} \log(\kappa) \right] \times |E|^2 d\sigma. \quad (\text{F20})$$

Furthermore, we exploit the periodicity $G(\sigma) = G(\sigma + T)$, as we investigate the long cavity regime. As the timescale of the absorber relaxation is much faster than the gain, it fully recovers between the passing of two pulses [see Eqs. (F10)–(F13)]. Utilizing these arguments, we arrive at the following algebraic expression for the integral in Eq. (F20):

$$\mathcal{I}_n = \frac{G_{i1}^{(n)} + G_{i2}^{(n)}}{2} (1 - e^{-P_n}) - \frac{Q_0}{2s} (1 - e^{-2sP_n}) + \frac{1}{2} \log(\kappa) P_n. \quad (\text{F21})$$

Inserting the equations for the gain before the first and second depletions ($G_{i1}^{(n)}$, $G_{i2}^{(n)}$) found from the system of algebraic equations [see Eqs. (F1)–(F9)] and the expression for Δ_{PC_2} , Eq. (9), into Eq. (F21) and solving for the normalized gain $g = G_0/G_{th}$, results in the following

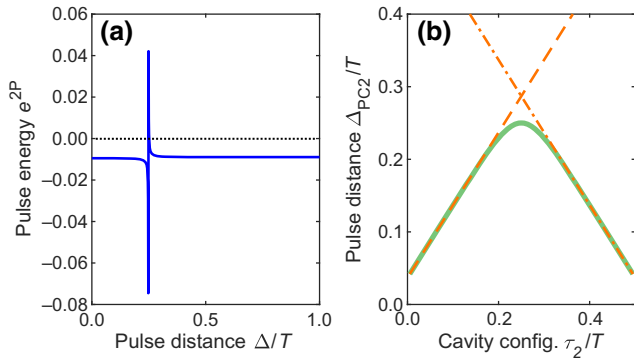


FIG. 12. (a) Relationship between the pulse power P and pulse distance Δ given by Eq. (F15), plotted for $T = 1.875$ ns, $\tau_2 = 0.474T$, and $\gamma_g = 5$ ns $^{-1}$. (b) Solution for the pulse distance Δ_{PC_2} for the PC_2 solution plotted in green, and the asymptotic behavior for $\tau_2 \rightarrow 0, T/2$ in orange.

equation relating the pulse power and gain value:

$$\begin{aligned}
 g(x) = & -4(e^{\gamma_g T} x^2 - 1) \left[\frac{Q_0(1 - x^{-s})}{2s} - \frac{1}{4} \log(x) \log(\kappa) \right] \\
 & \times \left\{ (\sqrt{x} - 1) [2Q_0 - \log(\kappa)] \right. \\
 & \times \left[2 + \frac{\sqrt{2}(\sqrt{x} - 1) 2e^{(1/2)\gamma_g(T-2\tau_2)}}{\sqrt{1 + e^{\gamma_g(T-4\tau_2)}}} \right. \\
 & + \frac{\sqrt{2}(\sqrt{x} - 1) x e^{(3/2)\gamma_g(T-2\tau_2)}}{\sqrt{1 + e^{\gamma_g(T-4\tau_2)}}} \\
 & + \frac{\sqrt{2}(\sqrt{x} - 1) x e^{(1/2)\gamma_g(T+2\tau_2)}}{\sqrt{1 + e^{\gamma_g(T-4\tau_2)}}} - 2e^{\gamma_g T} x^{3/2} \\
 & \left. \left. + (x - \sqrt{x})(e^{\gamma_g(T-2\tau_2)} + e^{\gamma_g 2\tau_2}) \right] \right\}^{-1}. \tag{F22}
 \end{aligned}$$

Here $x = e^{2P}$ with all other parameters as before.

The characteristics of the folding point of the PC_2 solution can also be reproduced by applying analytical expression (F22) for different τ_2 values. Differences might appear due to the fact that the out-coupling losses are very low and hence New's approximation is not perfectly accurate.

[1] H. A. Haus, Mode-locking of lasers, *IEEE J. Sel. Top. Quantum Electron.* **6**, 1173 (2000).
 [2] D. Waldburger, S. M. Link, M. Mangold, C. G. E. Alfieri, E. Gini, M. Golling, B. W. Tilma, and U. Keller, High-power 100 fs semiconductor disk lasers, *Optica* **3**, 844 (2016).

[3] M. Marconi, J. Javaloyes, S. Balle, and M. Giudici, How Lasing Localized Structures Evolve out of Passive Mode Locking, *Phys. Rev. Lett.* **112**, 223901 (2014).
 [4] P. Camelin, J. Javaloyes, M. Marconi, and M. Giudici, Electrical addressing and temporal tweezing of localized pulses in passively-mode-locked semiconductor lasers, *Phys. Rev. A* **94**, 063854 (2016).
 [5] J. K. Jang, M. Erkintalo, S. Coen, and S. G. Murdoch, Temporal tweezing of light through the trapping and manipulation of temporal cavity solitons, *Nat. Commun.* **6**, 7370 (2015).
 [6] M. Marconi, J. Javaloyes, P. Camelin, D. C. González, S. Balle, and M. Giudici, Control and generation of localized pulses in passively mode-locked semiconductor lasers, *IEEE J. Sel. Top. Quantum Electron.* **21**, 30 (2015).
 [7] F. Kurtz, C. Ropers, and G. Herink, Resonant excitation and all-optical switching of femtosecond soliton molecules, *Nat. Photonics* **14**, 9 (2019).
 [8] J. Wu, R. Keolian, and I. Rudnick, Observation of a Non-propagating Hydrodynamic Soliton, *Phys. Rev. Lett.* **52**, 1421 (1984).
 [9] E. Moses, J. Fineberg, and V. Steinberg, Multistability and confined traveling-wave patterns in a convecting binary mixture, *Phys. Rev. A* **35**, 2757 (1987).
 [10] S. Fauve and O. Thual, Solitary Waves Generated by Subcritical Instabilities in Dissipative Systems, *Phys. Rev. Lett.* **64**, 282 (1990).
 [11] E. Picholle, C. Montes, C. Leycuras, O. Legrand, and J. Botineau, Observation of Dissipative Superluminescent Solitons in a Brillouin Fiber Ring Laser, *Phys. Rev. Lett.* **66**, 1454 (1991).
 [12] F. J. Niedernostheide, M. Arps, R. Dohmen, H. Willebrand, and H. G. Purwins, Spatial and spatio-temporal patterns in pnpn semiconductor devices, *Phys. Status Solidi B* **172**, 249 (1992).
 [13] E. V. Vanin, A. I. Korytin, A. M. Sergeev, D. Anderson, M. Lisak, and L. Vázquez, Dissipative optical solitons, *Phys. Rev. A* **49**, 2806 (1994).
 [14] K. J. Lee, W. D. McCormick, J. E. Pearson, and H. L. Swinney, Experimental observation of self-replicating spots in a reaction-diffusion system, *Nature* **369**, 215 (1994).
 [15] P. B. Umbanhowar, F. Melo, and H. L. Swinney, Localized excitations in a vertically vibrated granular layer, *Nature* **382**, 793 (1996).
 [16] Y. A. Astrov and H. G. Purwins, Plasma spots in a gas discharge system: Birth, scattering and formation of molecules, *Phys. Lett. A* **283**, 349 (2001).
 [17] F. Gustave, L. Columbo, G. Tissoni, M. Brambilla, F. Prati, B. Kelleher, B. Tykalewicz, and S. Barland, Dissipative Phase Solitons in Semiconductor Lasers, *Phys. Rev. Lett.* **115**, 043902 (2015).
 [18] X. Yi, Q. F. Yang, K. Y. Yang, and K. Vahala, Imaging soliton dynamics in optical microcavities, *Nat. Commun.* **9**, 3565 (2018).
 [19] S. Barland, J. R. Tredicce, M. Brambilla, L. A. Lugiato, S. Balle, M. Giudici, T. Maggipinto, L. Spinelli, G. Tissoni, T. Knödl, M. Miller, and R. Jäger, Cavity solitons as pixels in semiconductor microcavities, *Nature* **419**, 699 (2002).
 [20] Y. Tanguy, T. Ackemann, W. J. Firth, and R. Jäger, Realization of a Semiconductor-Based Cavity Soliton Laser, *Phys. Rev. Lett.* **100**, 013907 (2008).

- [21] N. N. Akhmediev and A. Ankiewicz, *Dissipative Solitons*, Lecture Notes in Physics, Vol. 1 (Springer, Berlin, Heidelberg, 2005).
- [22] P. Grelu and N. N. Akhmediev, Dissipative solitons for mode-locked lasers, *Nat. Photonics* **6**, 84 (2012).
- [23] L. A. Lugiato, Introduction to the feature section on cavity solitons: An overview, *IEEE J. Quantum Electron.* **39**, 193 (2003).
- [24] T. Ackemann, W. J. Firth, and G. L. Oppo, in *Advances in Atomic Molecular and Optical Physics* (Academic Press, London, 2009), Vol. 57, Chap. 6, p. 323.
- [25] M. Marconi, J. Javaloyes, S. Barland, S. Balle, and M. Giudici, Vectorial dissipative solitons in vertical-cavity surface-emitting lasers with delays, *Nat. Photonics* **9**, 450 (2015).
- [26] S. Barland, S. Coen, M. Erkintalo, M. Giudici, J. Javaloyes, and S. Murdoch, Temporal localized structures in optical resonators, *Adv. Phys.* **X 2**, 496 (2017).
- [27] T. Herr, V. Brasch, J. D. Jost, C. Wang, N. Kondratiev, M. Gorodetsky, and T. Kippenberg, Temporal solitons in optical microresonators, *Nat. Photonics* **8**, 145 (2014).
- [28] M. Brambilla, T. Maggipinto, G. Patera, and L. Columbo, Cavity Light Bullets: Three-Dimensional Localized Structures in a Nonlinear Optical Resonator, *Phys. Rev. Lett.* **93**, 203901 (2004).
- [29] A. S. Pimenov, A. G. Vladimirov, S. V. Gurevich, K. Panajotov, G. Huyet, and M. Tlidi, Delayed feedback control of self-mobile cavity solitons, *Phys. Rev. A* **88**, 053830 (2013).
- [30] J. Javaloyes, Cavity Light Bullets in Passively Mode-Locked Semiconductor Lasers, *Phys. Rev. Lett.* **116**, 043901 (2016).
- [31] S. V. Gurevich and J. Javaloyes, Spatial instabilities of light bullets in passively-mode-locked lasers, *Phys. Rev. A* **96**, 023821 (2017).
- [32] D. Waldburger, C. G. E. Alfieri, S. M. Link, S. Meinecke, L. C. Jaurigue, K. Lüdge, and U. Keller, Multipulse instabilities of a femtosecond SESAM-modelocked VECSEL, *Opt. Express* **26**, 21872 (2018).
- [33] J. Hausen, S. Meinecke, B. Lingnau, and K. Lüdge, Pulse Cluster Dynamics in Passively Mode-Locked Semiconductor Vertical-External-Cavity Surface-Emitting Lasers, *Phys. Rev. Appl.* **11**, 044055 (2019).
- [34] M. Großmann, R. Bek, M. Jetter, and P. Michler, Stable fundamental and dual-pulse mode locking of red-emitting VECSELs, *Laser Phys. Lett.* **17**, 065001 (2020).
- [35] J. Javaloyes, M. Marconi, and M. Giudici, Nonlocality Induces Chains of Nested Dissipative Solitons, *Phys. Rev. Lett.* **119**, 033904 (2017).
- [36] L. Gui, P. Wang, Y. Ding, K. Zhao, C. Bao, X. Xiao, and C. Yang, Soliton molecules and multisoliton states in ultrafast fibre lasers: Intrinsic complexes in dissipative systems, *Appl. Sci.* **8**, 201 (2018).
- [37] W. Weng, R. Bouchand, E. Lucas, E. Obrzud, T. Herr, and T. Kippenberg, Heteronuclear soliton molecules in optical microresonators, *Nat. Commun.* **11**, 2402 (2020).
- [38] B. Ortac, A. Zavyalov, C. Nielsen, O. Egorov, R. Iliw, J. Limpert, F. Lederer, and A. Tünnermann, Generation of soliton molecules with independently evolving phase in a mode-locked fiber laser, *Opt. Lett.* **35**, 1578 (2010).
- [39] A. Zavyalov, R. Iliw, O. Egorov, and F. Lederer, Dissipative soliton molecules with independently evolving or flipping phases in mode-locked fiber lasers, *Phys. Rev. A* **80**, 043829 (2009).
- [40] Z. Wang, K. Nithyanandan, A. Coillet, P. Tchofo-Dinda, and P. Grelu, Optical soliton molecular complexes in a passively mode-locked fibre laser, *Nat. Commun.* **10**, 1 (2019).
- [41] M. Stratmann, T. Pagel, and F. Mitschke, Experimental Observation of Temporal Soliton Molecules, *Phys. Rev. Lett.* **95**, 143902 (2005).
- [42] A. Hause, H. Hartwig, M. Böhm, and F. Mitschke, Binding mechanism of temporal soliton molecules, *Phys. Rev. A* **78**, 063817 (2008).
- [43] K. Krupa, K. Nithyanandan, U. Andral, P. Tchofo-Dinda, and P. Grelu, Real-Time Observation of Internal Motion within Ultrafast Dissipative Optical Soliton Molecules, *Phys. Rev. Lett.* **118**, 243901 (2017).
- [44] G. Herink, F. Kurtz, B. Jalali, D. R. Solli, and C. Ropers, Real-time spectral interferometry probes the internal dynamics of femtosecond soliton molecules, *Science* **356**, 50 (2017).
- [45] P. Genevet, S. Barland, M. Giudici, and J. Tredicce, Cavity Soliton Laser Based on Mutually Coupled Semiconductor Microresonators, *Phys. Rev. Lett.* **101**, 123905 (2008).
- [46] F. Leo, S. Coen, P. Kockaert, S. P. Gorza, P. Emplit, and M. Haelterman, Temporal cavity solitons in one-dimensional Kerr media as bits in an all-optical buffer, *Nat. Photonics* **4**, 471 (2010).
- [47] B. Garbin, J. Javaloyes, G. Tissoni, and S. Barland, Topological solitons as addressable phase bits in a driven laser, *Nat. Commun.* **6**, 5915 (2015).
- [48] M. Pang, W. He, X. Jiang, and P. S. J. Russell, All-optical bit storage in a fibre laser by optomechanically bound states of solitons, *Nat. Photonics* **10**, 454 (2016).
- [49] P. Rohrmann, A. Hause, and F. Mitschke, Solitons beyond binary: Possibility of fibre-optic transmission of two bits per clock period, *Sci. Rep.* **2**, 866 (2012).
- [50] O. V. Yushko, A. A. Redyuk, M. P. Fedoruk, and S. Turitsyn, Coherent soliton communication lines, *J. Exp. Theor. Phys.* **119**, 787 (2014).
- [51] F. Mitschke, A. Hause, and C. Mahnke, Soliton molecules for advanced optical telecommunications, *Eur. Phys. J. Spec. Top.* **225**, 2453 (2016).
- [52] A. Schliesser, N. Picqué, and T. W. Hänsch, Mid-infrared frequency combs, *Nat. Photonics* **6**, 440 (2012).
- [53] Y. K. Chembo, D. V. Strekalov, and N. Yu, Spectrum and Dynamics of Optical Frequency Combs Generated with Monolithic Whispering Gallery Mode Resonators, *Phys. Rev. Lett.* **104**, 103902 (2010).
- [54] A. Coillet, J. M. Dudley, G. Genty, L. Larger, and Y. K. Chembo, Optical rogue waves in whispering-gallery-mode resonators, *Phys. Rev. A* **89**, 013835 (2014).
- [55] M. Tlidi, K. Panajotov, M. Ferré, and M. G. Clerc, Drifting cavity solitons and dissipative rogue waves induced by time-delayed feedback in Kerr optical frequency comb and in all fiber cavities, *Chaos* **27**, 114312 (2017).

- [56] F. Pedaci, G. Tissoni, S. Barland, M. Giudici, and J. R. Tredicce, Mapping local defects of extended media using localized structures, *Appl. Phys. Lett.* **93**, 111104 (2008).
- [57] C. Kerse, H. Kalaycioglu, P. Elahi, B. Cetin, D. K. Kesim, O. Akcaalan, S. Yavas, M. D. Asik, B. Öktem, H. Hoogland, R. Holzwarth, and F. Ilday, Ablation-cooled material removal with ultrafast bursts of pulses, *Nature* **537**, 84 (2016).
- [58] A. G. Vladimirov, A. S. Pimenov, and D. Rachinskii, Numerical study of dynamical regimes in a monolithic passively mode-locked semiconductor laser, *IEEE J. Quantum Electron.* **45**, 462 (2009).
- [59] J. N. Kutz, B. Collings, K. Bergman, and W. H. Knox, Stabilized pulse spacing in soliton lasers due to gain depletion and recovery, *IEEE J. Quantum Electron.* **34**, 1749 (1998).
- [60] C. Schelte, J. Javaloyes, and S. V. Gurevich, Dynamics of temporally localized states in passively mode-locked semiconductor lasers, *Phys. Rev. A* **97**, 053820 (2018).
- [61] K. Engelborghs, T. Luzyanina, and D. Roose, Numerical bifurcation analysis of delay differential equations using DDE-BIFTOOL, *ACM Trans. Math. Softw.* **28**, 1 (2002).
- [62] C. A. Klausmeier, Floquet theory: A useful tool for understanding nonequilibrium dynamics, *Theor. Ecol.* **1**, 153 (2008).
- [63] P. Camelin, C. Schelte, A. Verschelde, A. Garnache, G. Beaudoin, I. Sagnes, G. Huyet, J. Javaloyes, S. V. Gurevich, and M. Giudici, Temporal localized structures in mode-locked vertical external-cavity surface-emitting lasers, *Opt. Lett.* **43**, 5367 (2018).
- [64] H. A. Haus, Mode-locking of lasers, *IEEE J. Sel. Top. Quantum Electron.* **6**, 1173 (2000).
- [65] A. G. Vladimirov, A. S. Pimenov, S. V. Gurevich, K. Panajotov, E. Averlant, and M. Tlidi, Cavity solitons in vertical-cavity surface-emitting lasers, *Philos. Trans. R. Soc. Lond., Ser. A* **372**, 20140013 (2014).
- [66] A. S. Pimenov, S. Slepneva, G. Huyet, and A. G. Vladimirov, Dispersive Time-Delay Dynamical Systems, *Phys. Rev. Lett.* **118**, 193901 (2017).
- [67] C. Schelte, P. Camelin, M. Marconi, A. Garnache, G. Huyet, G. Beaudoin, I. Sagnes, M. Giudici, J. Javaloyes, and S. V. Gurevich, Third Order Dispersion in Time-Delayed Systems, *Phys. Rev. Lett.* **123**, 043902 (2019).
- [68] T. Kolokolnikov, M. Nizette, T. Erneux, N. Joly, and S. Bielawski, The q -switching instability in passively mode-locked lasers, *Physica D* **219**, 13 (2006).
- [69] C. Schelte, J. Javaloyes, and S. V. Gurevich, Functional mapping for passively mode-locked semiconductor lasers, *Opt. Lett.* **43**, 2535 (2018).
- [70] C. Schelte, D. Hessel, J. Javaloyes, and S. V. Gurevich, Dispersive Instabilities in Passively Mode-Locked Integrated External-Cavity Surface-Emitting Lasers, *Phys. Rev. Appl.* **13**, 054050 (2020).
- [71] A. G. Vladimirov and D. V. Turaev, Model for passive mode locking in semiconductor lasers, *Phys. Rev. A* **72**, 033808 (2005).
- [72] J. Hausen, K. Lüdge, S. V. Gurevich, and J. Javaloyes, How carrier memory enters Haus equation of mode-locking, *Opt. Lett.* (2020).
- [73] H. Uecker, D. Wetzel, and J. Rademacher, pde2path – A matlab package for continuation and bifurcation in 2D elliptic systems, *Numer. Math. Theor. Meth. Appl.* **7**, 58 (2014).
- [74] G. Giacomelli and A. Politi, Relationship between Delayed and Spatially Extended Dynamical Systems, *Phys. Rev. Lett.* **76**, 2686 (1996).
- [75] G. New, Pulse evolution in mode-locked quasi-continuous lasers, *IEEE J. Quantum Electron.* **10**, 115 (1974).